The International Journal of Advanced Manufacturing Technology (2023) 124:1925–1938
https://doi.org/10.1007/s00170-022-10562-z

ORIGINAL ARTICLE

A novel approach for the numerical analysis of in situ distortion in a component made by the directed energy deposition additive manufacturing process

Pegah Pourabdollah[1] · Farzaneh Farhang Mehr[1] · Daan M. Maijer[1] · Steven L. Cockcroft[1]

Received: 5 August 2022 / Accepted: 17 November 2022 / Published online: 7 December 2022

Abstract
Developing a fundamental understanding of the in situ deformation and residual stress development during additive manufacturing (AM) processes is critical to controlling component deformation and, consequently, producing high-quality components. In this work, a macro-scale finite element (FE) model was developed to predict the thermo-mechanical response of a hollow rectangular during and after a directed energy deposition (DED) process. A layer agglomeration method using time-averaged heat input was applied in the model to speed up the computation. The novel features of the modeling methodology in this work include the following: (1) activating the deposited material at an initial temperature above the solidus to capture the generation of plastic strain as an alternative approach to introducing an inherent strain; (2) compensating for the enthalpy of the deposited material in the time-averaged volumetric heat input describing the laser; and (3) defining separate, material-centric, thermal strain evolution for the deposited material and the baseplate. The model predictions were validated against in situ experimental temperature and displacement data reported in the literature. A sensitivity analysis was conducted with the validated model to investigate the influence of preheating the baseplate, the initial temperature of the deposited material and the laser power on the baseplate temperature and distortion evolution. The results prove this novel simulation methodology to be an efficient way to predict a component's thermo-mechanical behaviour during the DED process.

Keywords Additive manufacturing (AM) · Directed energy deposition (DED) · Finite element numerical analysis · Residual stress · Mathematical modeling

1 Introduction

Directed energy deposition (DED) process is one of the most common additive manufacturing (AM) processes used to fabricate metallic components. This process allows a rapid build-up of components onto substrates or previously deposited and consolidated layers [1–3]. In the DED process, the feeding system moves together with the beam and introduces the feed material directly into the melt pool, depositing material in the desired location [4, 5]. The DED method provides unique capabilities relative to powder bed processes, including the ability to (i) add features to existing components, (ii) repair damaged or worn component surfaces and (iii) make parts with various materials during the same build [5–7].

One of the common issues in the DED process is that the fast movement of the heat source causes rapid heating and cooling and, consequently, substantial temperature gradients in the component being fabricated. These temperature gradients can result in yielding and the generation of plastic strain, leading to residual stresses and associated component distortion. The other source of residual stress is the thermal strain mismatch between the deposited material and the substrate material. Residual stresses can increase manufacturing costs due to part rejection and/or the necessity for subsequent operations such as machining or stress relief procedures [4, 5, 7–9]. Therefore, establishing a deep understanding of how various process parameters contribute to the development of residual stresses can help optimize the build process to control deformation, achieve dimensional accuracy and enhance the mechanical performance of the

✉ Daan M. Maijer
daan.maijer@ubc.ca

[1] Department of Materials Engineering, University of British Columbia, 6350 Stores Rd, Vancouver, BC V6T 1Z4, Canada

component. However, relying merely on experimental build trials can be expensive and time-consuming since various parameters, such as heat source power, layer thickness, scanning speed [8, 10, 11], scanning strategies [12] and substrate preheat temperature [13], can affect part deformation. Instead, limited experimental trials can be used to validate a mathematical model capable of describing the link between process parameters and the state of the final component. In turn, this model can be used to optimize the build process and reduce the number of experiments required to study each process parameter's effect [8, 13, 14].

Various studies [7, 11, 15–19] have reported that the computational time for predicting distortion and residual stress in DED fabricated parts can take days, weeks or months, depending on the geometry of the simulated part and the complexity of the model (e.g. moving heat source, nonlinear material properties and boundary conditions). Various researchers [7, 11, 14, 19–26] have explored strategies to reduce the computational time of thermo-mechanical analyses of AM processes, including the layer agglomeration/lumping, flash heating, and inherent strain methods. Among these researchers, Liang et al. [7], Lu et al. [11], Wang et al. [25] and Kiran et al. [17] have focused their work on the computational efficiency of simulating the DED process. In each approach, specific limitations have been identified that will be reviewed.

In the agglomeration method, several layers are lumped into one computational "super layer" to reduce computational time [11, 14, 21]. For example, Lu et al. [11] developed a fully coupled thermo-mechanical model using the COMET[1] software to predict the evolution of stress and distortion in an S-shaped component and a hollow rectangular part, each made of 44 layers by a laser-based DED system. The model was validated using the in situ distortion and temperature measurements obtained at different locations on the bottom of the baseplate. Although the predicted results were in good agreement with the experimental measurements, the model was computationally expensive. Therefore, Lu et al. [11] simplified the thermo-mechanical model by using the agglomeration method for element activation and by incorporating a modified moving heat source. The simplified model reduced the computational time, but the predicted temperatures and displacements exhibited large oscillations that were inconsistent with the measurements [11].

The flash heating method is a thermal modeling approach that can be combined with the agglomeration method to further reduce computational time. Instead of modeling the precise details of the heat source-material interaction, this method applies an equivalent uniform heat source to each super layer [11, 17, 25]. Kiran et al. [17] developed a thermo-mechanical model using the flash heating and agglomeration methods to predict the residual stress in a 316L stainless steel 3D cubic structure manufactured by the DED process. They examined different numbers of lumped layers to strike a balance between maintaining model accuracy and reducing computational time. The authors reported good agreement between model predictions and experimental results. However, they appear to have used an unrealistically high heat input to reach the material's melting temperature to compensate for the fact that they apply a uniform heat flux to the whole surface of multiple layers activated simultaneously. In another work, Wang et al. [25] established a thermo-mechanical model based on a line-based flash heating method with different scaling strategies to simulate the part-scale DED process. This method considered the overlap and scanning strategy parameters. They concluded that increasing the loading volume in this method results in lower calculation costs but larger deformation prediction errors.

The inherent strain method was initially developed to enable rapid prediction of residual stresses in welding processes [27]. In this method, the inherent strain in the component is determined from experimental calibrations or small-scale thermo-mechanical simulations. The inherent strain tensor is then applied uniformly to a macro-scale mechanical model of the full part to predict the part's distortion and stress state [14]. In 2014, Keller and Ploshikhin [19] adapted and used this method to rapidly predict the distortion of laser powder bed fusion (L-PBF) parts. Although their model is computationally fast, obtaining good accuracy in the part-scale distortion prediction was challenging. Liang et al. [7] proposed a modified inherent strain method to rapidly predict the distortion of parts fabricated by the DED process. The inherent strains were estimated from a detailed process simulation of single-line depositions on top of each other. These strains were then applied to a layer-by-layer static equilibrium analysis to predict the full part's residual stress and distortion. The results showed that the modified inherent strain method efficiently predicted the part's distortion. However, the limitation of this model is that it can only estimate the inherent strains in single-pass, straight-line depositions.

The current work will present a unique modeling approach to predict the macro-scale, in situ and ex situ thermo-mechanical responses of a laser-based, powder-fed DED process, which allows the analyses of large, complex components in a relatively short period of time. The model adopts the layer agglomeration method, which is a common method to reduce computational time. The following novel techniques were utilized in this model:

1. A time-averaged volumetric heat input was used to describe the energy input to avoid the computational

[1] A co-design engineering toolset for hardware, software and mechanical modeling.

Table 1 Summary of physical and super layer process parameters [11]

Parameters	Physical layer	Super layer
Deposited layer thickness (mm)	0.49	1.96
Number of build layers	44	11
Laser power (W)	1500	1500
Total time per layer (s)	25	100
Heating time per layer (s)	20	-
Time between processing two consecutive layers (s)	5	-
Scanning speed (mm s^{-1})	10	-
Feeding rate (g min^{-1})	12	-

overhead associated with tracking the motion of the beam.

2. The deposited material was added at an initial temperature above solidus to capture the generation of plastic strain as an alternative approach to introducing an inherent strain.
3. To ensure the conservation of energy, the energy associated with adding the deposited material at an elevated temperature was deducted from the energy input associated with the laser.
4. Material-centric thermal strain evolution was implemented to correctly capture the difference in strain history exhibited by the baseplate and deposited material.

The model predictions were validated against in situ temperature and displacement data reported by Lu et al. [11] for a hollow rectangular component. Furthermore, the validated model was used to investigate the influence of process parameters on the baseplate's thermal behaviour and distortion evolution.

2 Model development

A 3D, transient, thermo-mechanical model has been developed in ABAQUS,[2] a commercial finite element analysis tool, to predict the thermo-mechanical response of a part during and after a laser-based powder-fed DED process. The model adopted a fully coupled approach to facilitate data handling. It is important to note that the problem can be solved with a weakly coupled strategy, as the displacement field does not impact heat transport. The energy balance and stress equilibrium equations are solved to calculate the temperature and stress/strain/distortion fields, respectively.

To reduce the computational size of the problem, the layer agglomeration approach has been used in which every four physical process layers are lumped into one computational super layer. This is equivalent to changing the powder layer thickness from 0.49 to 1.96 mm. Table 1 summarizes the process parameters employed in the experiment and the equivalent parameters used in the model. For example, the total time to process each layer is 25 s in the actual experiment, which includes the heating time per layer (20 s) and the time between processing two consecutive layers (5 s). The total time for processing each super layer in the computational model, including the deposition and cooling times, is therefore, 100 s (4 × 25 s), based on the thickness of the super layer compared to the thickness of the physical process layer. In the time-averaged heat input approach, there is no distinction between the heating time per layer and the time between processing two consecutive layers.

The initial, minimum, and maximum timesteps were set to 0.001 s, 10^{-5} s, and 1 s, respectively. In addition, the maximum temperature change per increment was set to 5 ℃. As noted above, the solution depends only on integrating the heat transport equations.

2.1 Geometry and finite element mesh

The computational domain includes 3D representations of the baseplate and the part (hollow rectangle) geometries. Figure 1 shows dimensioned drawings of the baseplate and part and an isometric view of the meshed domain. The baseplate and part geometries were based on the previous study [11].

In this model, the part was partitioned vertically in the z-direction into 11 layers, each representing the agglomeration of 4 physical process layers. The domain was meshed with 3D coupled temperature-displacement hexagonal elements (C3D8RT[3]). Each computational layer of the part was meshed with 1 element in the height direction and contained 822 nodes and 311 elements. In total, there were 12,621 nodes and 9208 elements in the model.

2.1.1 Addition of elements

The sequential deposition of material poses a significant challenge when simulating AM processes. Researchers have proposed various strategies for modeling the addition of elements in AM processes [24, 28]. In this work, the deactivate/activate strategy was used in which all of the nodes and elements in the domain are initialized in the model. To begin the analysis, all of the elements in the component

[2] ABAQUS is the trademark for Dassault Systèmes.

[3] Eight-node trilinear displacement and temperature reduced integration with hourglass control.

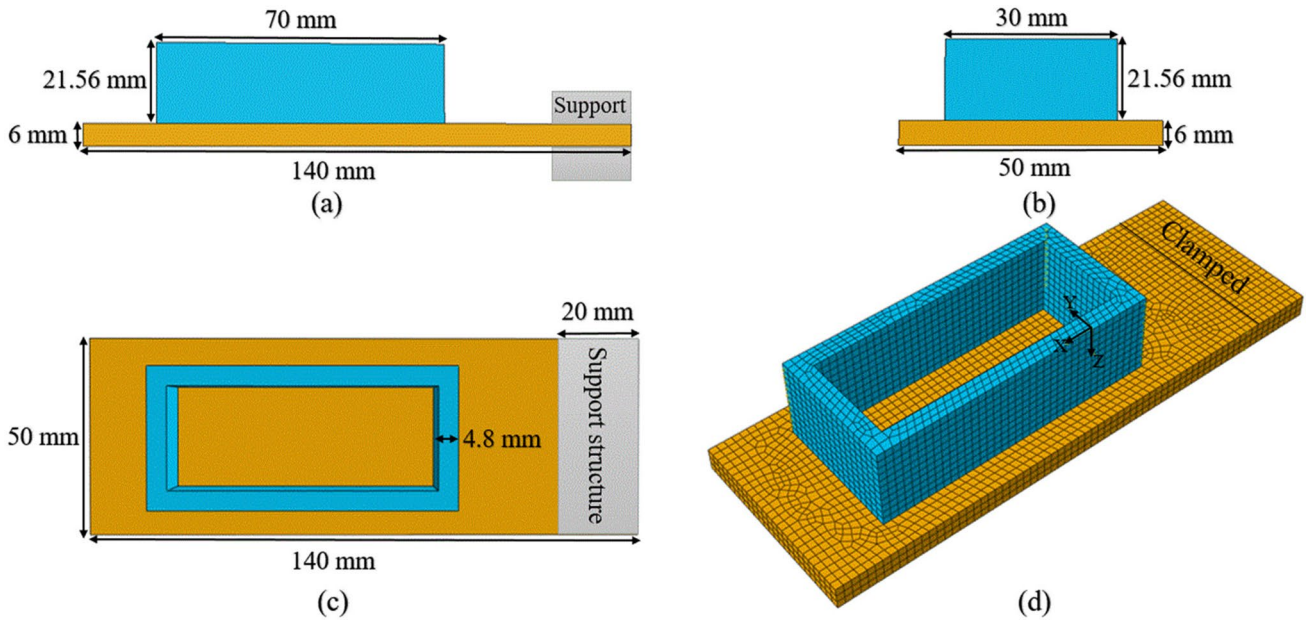

Fig. 1 The dimensioned 2D drawing of the geometry (**a**) Front, (**b**) side, and (**c**) top views and the 3D solution domain (**d**) isometric view

are deactivated. The layers of elements of the part are then sequentially reactivated step by step for each computational layer. In the current work, short transition steps were used in ABAQUS to deactivate (0.001 s in duration) and reactivate (0.001 s in duration) the elements. From the standpoint of the thermal analysis, when the elements are reactivated, only the new nodes added to the computational domain are activated at the initial temperature. Likewise, in the stress analysis, only the new nodes are activated at the original mesh coordinates. The result is that the newly activated layer is deformed. However, the elements are added strain-free, an option available in ABAQUS.

2.2 Governing equations

2.2.1 Thermal

The 3D transient heat balance equation used to compute the temperature field in the domain is shown in Eq. 1.

$$\frac{\partial}{\partial x}\left(k\frac{\partial T}{\partial x}\right)+\frac{\partial}{\partial y}\left(k\frac{\partial T}{\partial y}\right)+\frac{\partial}{\partial z}\left(k\frac{\partial T}{\partial z}\right)+\dot{Q}=\frac{\partial\left(\rho C_P T\right)}{\partial t} \tag{1}$$

where k is the thermal conductivity (W m^{-1} K^{-1}), T is the temperature (K), $\dot{Q}$ is the rate of volumetric heat input (W m^{-3}), ρ is the density (kg m^{-3}), C_p is the specific heat capacity (J kg^{-1} K^{-1}), t is time (s) and x, y and z are the coordinates (m).

A unique approach has been adopted to define a time-averaged volumetric heat source, which is introduced in the top layer of elements over the processing time taken to deposit a computational layer (i.e. corresponding to four deposition layers in the process). In this approach, the heat input from the laser has been reduced to account for the elevated deposition temperature of the material being added. The rate of enthalpy input associated with the deposited material is calculated as per Eq. 2.

$$\dot{Q}_{\text{Enthalpy}}=\frac{\dot{M}_{\text{Deposition}}\left(C_{\text{p}}\left(T_{\text{Deposition}}-T_{\text{Powder}}\right)+L\right)}{V_{\text{CompLayer}}} \tag{2}$$

where $\dot{Q}_{\text{Enthalpy}}$ is the rate of heat input associated with material that is deposited at an elevated temperature (W m^{-3}), $\dot{M}_{\text{Deposition}}$ is the mass deposition rate (kg s^{-1}), $T_{\text{Deposition}}$ is the temperature of the deposited material (K), T_{Powder} is the initial temperature of the powder fed into the process, L is the latent heat of melting (J kg^{-1}) and $V_{\text{CompLayer}}$ is the volume of the elements in the activated computational layer (m^3). This approach allows the deposited material to be added at temperatures above the melting point, consistent with the process where the material being deposited is molten, while ensuring that the total heat input in the model is consistent with the actual process input energy. The resulting expression for the time-averaged heat input is given below in Eq. 3.

$$\dot{Q}_{\text{Avg}}=\left(\eta\dot{Q}_{\text{Beam}}-\dot{Q}_{\text{Enthalpy}}\right)\frac{t_{\text{Deposition}}}{t_{\text{Total}}} \tag{3}$$

where $\dot{Q}_{\text{Avg}}$ is the rate of time-averaged volumetric heat input (W m^{-3}); $t_{\text{Deposition}}$ is the time that the laser heats the part

during the deposition of four layers in the process; t_{Total} is the total time to process the four layers, including the time for repositioning the deposition/laser head between layers; $\dot{Q}_{\text{Beam}}$ is the rate of heat input from the laser (W m^{-3}); and η is the absorptivity of the material being heated/efficiency of heating, which was set to 0.37 [11]. $\dot{Q}_{Beam}$ is calculated as the laser power divided by the volume of the elements in the super layer being processed.

2.2.2 Mechanical

The mechanical analysis predicts the deformation of the component during and after the DED process. The governing stress equilibrium equation that is solved to determine the deformation is as follows:

$$\nabla \bullet \sigma + b = 0 \tag{4}$$

where σ is the Cauchy stress tensor, and b is the body force vector. A stress–strain constitutive equation is required to relate stress, strain and material properties. The constitutive behaviour is given by the generalized Hooke's law as per Eq. 5.

$$\sigma_{ij} = C_{ijkl}\epsilon^{e}_{kl} \quad ; \quad i,j,k,l \in \{x,y,z\} \tag{5}$$

where ϵ^{e}_{kl} is the elastic strain tensor, and C_{ijkl} is the fourth-order material stiffness matrix, which is computed as a function of Young's modulus, E (Pa), and Poisson's ratio, ν, as per Eq. 6.

$$C_{ijkl} = \frac{E}{1+\nu}\left[\frac{1}{2}\left(\delta_{ik}\delta_{jl} + \delta_{jk}\delta_{il}\right) + \frac{\nu}{1-2\nu}\delta_{ij}\delta_{kl}\right] \tag{6}$$

where δ is a Dirac delta function whose value is one for $i = j$ and $l = k$, and is otherwise zero. The total strain tensor, ϵ^{tot}, is composed of four components, as shown in Eq. 7.

$$\epsilon^{\text{tot}} = \epsilon^{\text{e}} + \epsilon^{\text{p}} + \epsilon^{\text{th}} + \epsilon^{\text{V}} \tag{7}$$

where ϵ^{p} is the plastic strain, ϵ^{th} is the thermal strain and ϵ^{V} is the strain induced by a solid-state phase transformation and/or creep, which was ignored in this model. Thermal strains are induced by changes in temperature and can be calculated using Eq. 8 [29].

$$\epsilon^{\text{th}} = \alpha(T)\left(T - T_{\text{ref}}\right) - \alpha\left(T_{\text{i}}\right)\left(T_{\text{i}} - T_{\text{ref}}\right) \tag{8}$$

where α is the thermal expansion coefficient, T is the current temperature, T_{ref} is a reference temperature at which the thermal strain is assumed to be zero and T_i is the initial temperature. The plastic strain is calculated using the von Mises yield criterion and Prandtl-Reuss flow rule, as shown in Eqs. 9 and 10.

Table 2 Temperature-dependent thermo-physical properties of Ti64 [11]

T (°C)	ρ (kg m^{-3})	C_{p} (J kg^{-1} K^{-1})	k (W m^{-1} K^{-1})
25	4420	546	7
205	4395	584	8.75
500	4350	651	12.6
995	4282	753	22.7
1100	4267	641	19.3
1200	4252	660	21
1604	4198	732	25.8
1660	3886	831	83.5
2000	3818	831	83.5

$$\sigma_{\text{VM}} = \left[\frac{3}{2}\sigma_{ij}\sigma_{ij} - \frac{1}{2}(\sigma_{\text{kk}})^2\right]^{1/2} \tag{9}$$

$$d\varepsilon^{p} = \sigma' d\lambda \tag{10}$$

where σ_{VM} is the Von Mises stress, $d\lambda$ is a non-negative scalar constant of proportionality and σ' is the deviatoric stress. The material behaviour was assumed to be elastic-perfectly plastic.

2.3 Material properties

Since AM components experience a broad range of temperatures during their fabrication, employing temperature-dependent material properties is critical to accurately simulate the material's behaviour during processing. The temperature-dependent thermo-physical and mechanical properties of Ti-6Al-4 V (Ti64) used in the model are summarized in Tables 2 and 3, respectively. The data is available in the literature for a temperature range from 20 to 2000 °C. ABAQUS uses linear interpolation to determine the material properties at temperatures between the data points. The α/β-transus temperature range is 980–1010 °C. The solidus and liquidus temperatures are 1604 °C and 1660 °C, respectively. The latent heats of the α/β phase transformation and solidification are 48 and 286 (kJ kg^{-1}), respectively.

To better describe Ti64 behaviour during AM processing, the following assumptions were made:

1. The new nodes added to the domain are activated at a temperature above liquidus. Within the liquid pool that forms in the actual DED process, there is a potential for fluid flow (buoyancy and Marangoni-force driven) to enhance heat transport. To approximate the effect of enhanced heat transport in the regions above the liquidus temperature, the material's thermal conductivity above 1604 ℃ was enhanced by a factor of three [8, 11].

Table 3 Temperature-dependent mechanical properties of Ti64 [11]

T (°C)	α' (10^{-6} K^{-1})	$\alpha_{baseplate}$ (10^{-6} K^{-1})	$\alpha_{deposition}$ (10^{-6} K^{-1})	E (GPa)	σ_y (MPa)	ν
25	8.78	10	11.2	110	850	0.345
205	10	10.1	11.5	100	630	0.35
500	11.2	10.7	11.9	76	470	0.37
995	12.3	11.5	12.4	15	13	0.43
1100	12.4	11.6	12.4	5	5	0.43
1200	12.42	11.7	12.4	4	1	0.43
1604	12.5	0	0	1	0.5	0.43
1660	12.5	0	0	0.1	0.1	0.43
2000	12.5	0	0	0.01	0.01	0.43

The model's sensitivity to this adjustment was assessed and found to be negligible. This could be eliminated in future versions of the model.

2. Mechanical properties, such as Young's modulus and yield stress, are not measurable for material in the liquid state; however, to run the model, it is necessary to input a non-zero value for these properties at temperatures above the liquidus temperature. Therefore, Young's modulus and yield stress were assumed to drop to 0.01 GPa and 0.01 MPa, respectively, at temperatures above the liquidus [11].
3. The yield stress is assumed to decrease rapidly as temperatures increase from 500 to 1000 °C, indicating the high probability of plastic deformation during AM processes [11, 30]. In this work, the strain hardening behaviour and the effect of strain rates on the plastic behaviour of Ti64 were neglected as per Nasser et al.'s [31] suggestion that the flow stress of Ti64 is more dependent on temperature than the strain rate.

The coefficient of thermal expansion (CTE) is an important material property that significantly influences the evolution of stress and distortion in a thermo-mechanical model. It is possible to calculate the thermal strain via two methods: (1) using the instantaneous coefficient of thermal expansion (ICTE), $\alpha'(T)$, which is the tangent of the thermal strain versus temperature curve, and (2) using the secant coefficient of thermal expansion (SCTE), $\alpha(T)$, which defines the total thermal expansion coefficient from a reference temperature. Since ABAQUS uses the SCTE, the $\alpha'(T)$ reported in the literature was converted to $\alpha(T)$ using the following [29]:

$$\alpha(T) = \frac{1}{T - T_{\text{ref}}} \int_{T_{\text{ref}}}^{T} \alpha'(T) dT \tag{11}$$

Another challenging aspect of this work was correctly capturing the differential strain accumulation in the baseplate and the part. Thermal strains in the baseplate accumulate from the start of the process when the baseplate is at room temperature, while the material being deposited is added strain-free and will accumulate thermal strains as it cools. To implement this, the reference temperature for zero thermal strain in the baseplate was set to 25 °C, whereas, for the deposited material, the reference temperature for zero thermal strain was the solidus (e.g. 1604 °C), where the material is fully solidified and is capable of withstanding an applied load. Liquid metal will contract as it cools, but unless it is fully encapsulated by solid, it will flow without causing deformation in the surrounding solid regions. Thus, above the solidus temperature, the SCTE was set equal to zero for the deposited material to reflect the assumption that thermal strains leading to mechanical deformation are not generated in areas where the material is partially or completely liquid.

2.4 Initial conditions

At the start of the build process, the baseplate temperature was set to 25 °C based on the experimental conditions. The initial temperature of the material once it has been deposited in the part is unknown and difficult to measure experimentally or estimate based on the complicated interaction between the laser beam and the feed material (powder). In the current approach, the initial temperature of the computational layer upon activation was adjusted so that the predicted evolution in distortion is in good agreement with the measured in situ displacement data. Using a trial-and-error approach, an initial temperature of 2200 °C was found to yield acceptable results. The effect of the initial temperature of the computational layers on distortion is examined in section 3.

2.5 Boundary conditions

2.5.1 Thermal boundary conditions

During the laser-based DED process, the built part is heated via a laser and heat loss occurs through conduction to the

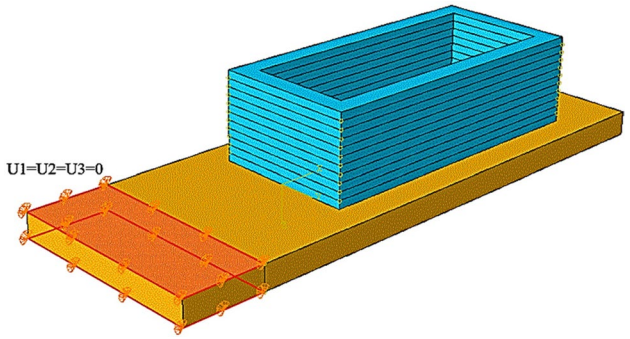

Fig. 2 Surface partitions on the baseplate where mechanical boundary conditions were applied

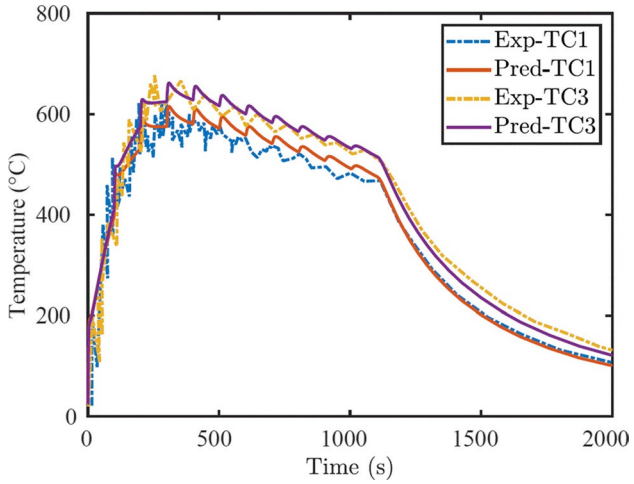

Fig. 3 Measured [11] and predicted thermal history at two locations on the bottom surface of the baseplate

connected baseplate and via convection and radiation to the surrounding environment. In addition to radiation and convection, the baseplate loses heat via conduction to the support structure that the baseplate is clamped to (refer to Fig. 1). As described earlier, laser heat input was treated as a volumetric heat source term in this work. A radiation boundary condition was applied to all free surfaces on the built part and baseplate using the Stephen-Boltzmann law, as shown in Eq. 12.

$$q''_{rad} = \varepsilon\sigma\left(T_s^4 - T_\infty^4\right) \tag{12}$$

where ε is the surface emissivity, which was set to 0.5 for outer walls and 0.285 for inner walls (inside the hollow rectangular part), σ is the Stefan-Boltzmann constant (5.67×10^{-8} W m^{-2} K^{-4}), T_s is the surface temperature and T_∞ is the ambient temperature (was set to 25 °C). The lower emissivity for inner walls is an effective emissivity accounting for the net effect of heat transfer between the inner walls of the built part.

The convective heat loss due to inert gas flow on the free surfaces was modelled using Newton's law of cooling, as shown in Eq. 13.

$$q''_{\text{conv}} = h\left(T_s - T_\infty\right) \tag{13}$$

where h is a heat transfer coefficient, which was set to 5 W m^{-2} K^{-1}, and T_∞ is the inert gas temperature, which was set to 25 °C.

Conductive heat loss between the baseplate and the support structure was also described using Eq. 13, but with an increased heat transfer coefficient of 50 W m^{-2} K^{-1}. The temperature of the support structure in contact with the baseplate was assumed to remain at 25 °C (e.g. $T_\infty = 25$ °C).

2.5.2 Mechanical boundary conditions

Mechanical boundary conditions are necessary to describe the constraints present during the build process. In this work, the baseplate was constrained at one end, creating a cantilevered plate, as described in the experimental setup [11]. The nodes on the top and bottom surface of the baseplate in the region that was in contact with the support structure were fixed in all directions. The portions of the top and bottom baseplate surfaces where these mechanical boundary conditions were applied are shown in Fig. 2.

3 Results and discussion

The model described in section 2 was run for an initial set of boundary conditions and an initial temperature of the deposited material. The predicted temperatures and displacements in the baseplate were compared to the experimental data reported in [11]. A trial-and-error process was employed to revise the heat transfer boundary conditions and determine the initial temperature of the deposited material for the model that matched the measurements. The model predictions will first be compared to the experimental measurements to develop confidence in the model accuracy. The model will then be used to examine the state of stress in the built part before conducting a sensitivity analysis on key process variables.

3.1 Temperature and deformation

The thermal history and vertical displacement of the baseplate obtained from the model have been compared to the in situ experimental measurements reported by Lu et al. [11]. Figure 3 shows a comparison between the measured and predicted temperature history at two locations on the bottom surface of the baseplate. The locations of the thermo-couples

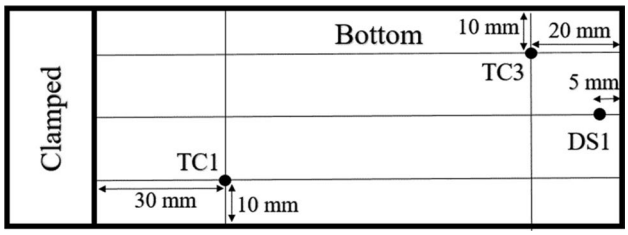

Fig. 4 The thermo-couple and displacement sensor locations on the bottom surface of the baseplate [11]

the measured data because of the use of the agglomeration technique. The quick temperature rise in the model predictions is due to the high initial temperature of new layers and the heat input. The results show that the model, regardless of using the agglomeration method and the time-averaged heat input, is able to predict thermal behaviour and is more accurate than the simplified model presented in [11].

Figure 5a shows a contour plot of the predicted displacement in the vertical direction once the built part and baseplate are cooled to a temperature close to room

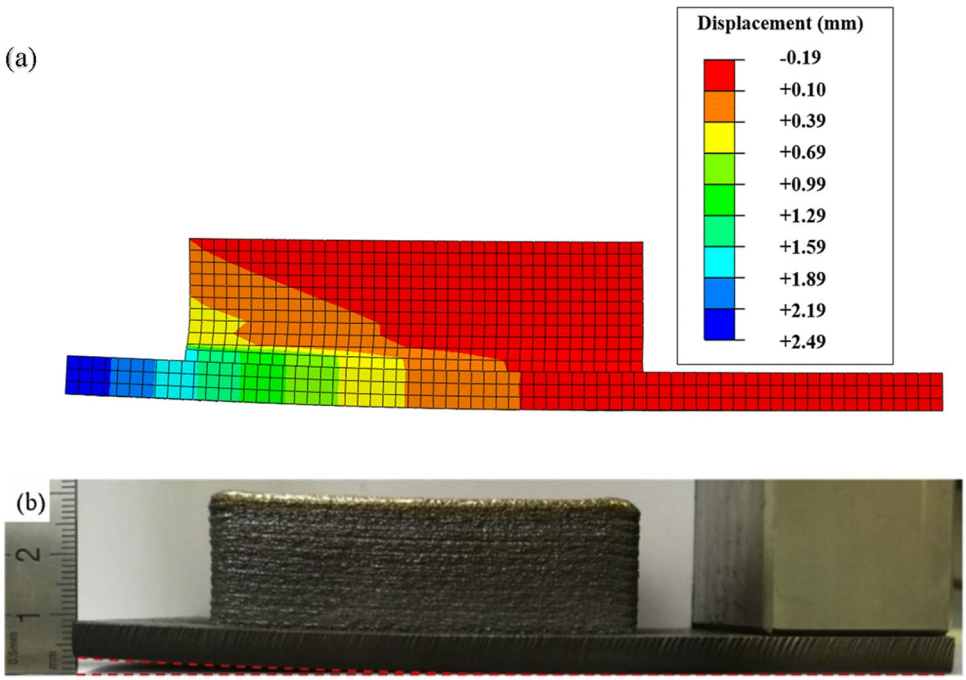

Fig. 5 Comparison of the (**a**) predicted and (**b**) actual [11] distorted shapes of the built part and baseplate

on the baseplate are shown in Fig. 4. Overall, there is good agreement between predicted and measured results.

The macro-scale thermal history of the baseplate can be divided into three stages. During the deposition of the first three computational layers (i.e. corresponding to twelve deposition layers in the process), the temperature increases rapidly from room temperature to peak temperature, which exceeds 600 °C. As deposition continues, the temperature gradually decreases as the distance from the thermo-couple locations to the new layers being added and the heat source increases. Once the part has reached the desired height, i.e. deposition is complete, the part is no longer heated, and the baseplate and part cool down.

At a finer time-scale, the temperatures of both the predicted and measured data clearly show regular, periodic, rapid rises followed by gradual decreases in temperature, which are associated with the addition of layers of material. The cycle of adding and processing layers of material in the model occurs less frequently than indicated by

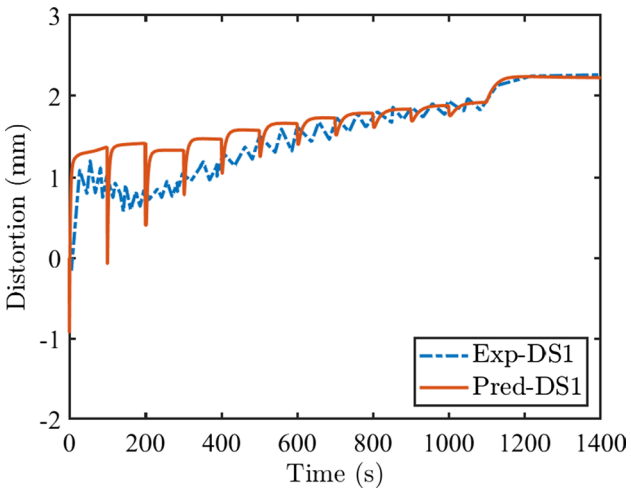

Fig. 6 The evolution of distortion of the bottom surface of the baseplate at DS1 from both experimental [11] and simulation results

temperature. The displacement contours have been plotted on the deformed grid. Figure 5b is an image of the baseplate and built part after fabrication showing the extent of the deformation. As can be seen, the model qualitatively predicts the same distortion behaviour observed experimentally.

Figure 6 compares the measured and predicted displacement history of the baseplate at displacement sensor 1 (DS1) (refer to Fig. 4 for location). The comparison shows excellent agreement at the end of fabrication when the built part and baseplate are thoroughly cooled, indicating that the model can quantitatively predict the final displacement of the baseplate. The predictions and measurements again show a periodicity associated with the incremental addition of each layer. For the model, the addition or activation of a new layer of "hot material" results in a sharp drop in displacement. This response is then followed by a rapid rise in displacement, which transitions to a continued slow increase in displacement until the next layer is added. This behaviour is related to the fluctuating thermal field associated with the addition of each layer of hot (2200 °C) material. The short-duration addition of each layer results in an increase in temperature and thermal expansion of the previously deposited material, causing the short-term, sharp drop in the displacement of the baseplate. The overall accumulation of negative thermal strain in the deposited material as it solidifies, cools and shrinks ultimately dominates the deformation response, driving the trend to increase the positive upward deformation of the built part and baseplate.

During the deposition of the first layer in the model, the large temperature gradient, induced by the addition of high-temperature elements directly on the baseplate, which is at room temperature, leads to a significant distortion in the baseplate, bending the baseplate and first layer upward. This stage is responsible for approximately 50% of the total deformation. The new nodes of the second layer are then activated at the original mesh coordinate, resulting in deformed elements, particularly on the left side, as seen in Fig. 5a. During the deposition of other layers, the distortion of the baseplate increases; however, the amount of distortion is smaller compared to after the deposition of the first layer, and as a result, the elements of other layers are less deformed compared to the elements of the second layer (Fig. 5a). During final cooling, which commences at approximately 1100 s, the distortion continues to increase. Roughly 20% of the total distortion is accumulated during the final cooling stage. Therefore, the distortion of the part is strongly affected by the large temperature gradients during material deposition and final cooling.

There is some mismatch between the measured and predicted results after the deposition of the first few layers due to the agglomeration method and the time-averaged heat input strategies adopted in the model. Moreover, the measurements show a section of time (50 to 150 s) where the displacement decreases, which is not captured in the predicted results. However, the error in the predictions decreases with increasing number of layers added. The final bending of the baseplate predicted by the model is 2.49 mm, which is in good agreement with the experimental measurement of 2.61 mm. The results indicate that this model can predict a component's distortion with acceptable accuracy. Furthermore, this model is less computationally intensive (it takes less than 10 min using 12, 2.33 GHz, Intel Quad core CPUs to produce results) and will require less computational time compared to the model presented in reference [11].

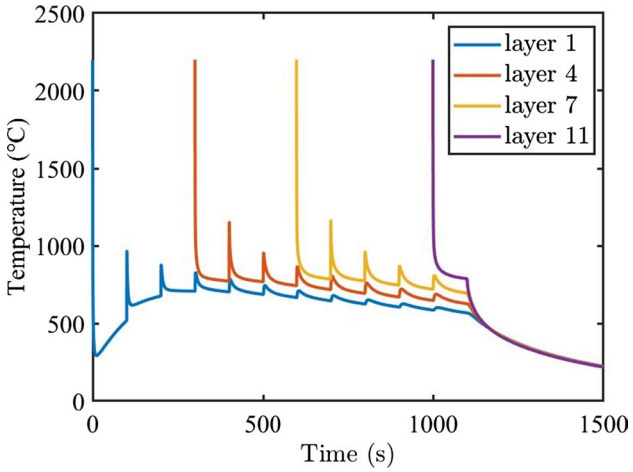

Fig. 7 The thermal history of locations at the top of layers 1, 4, 7 and 11

Figure 7 shows the thermal history of locations at the top of layers 1, 4, 7 and 11 in the built part. A rapid temperature decrease occurs immediately after the activation of each layer due to heat conduction to the baseplate and previously deposited layers. The temperature then gradually changes due to the time-averaged heat input and continued conduction to the material below. The temperature rise, and peaks associated with subsequent layer addition, diminishes with increasing layer addition because of the increasing distance from the heat input associated with each layer. During the deposition of the first layer, a large temperature gradient is induced in the cold baseplate, which is at room temperature. These temperature gradients lead to the formation of stresses and distortion.

3.2 Stress development

Figure 8 shows the evolution of the temperature, longitudinal stress in the *x*-direction (S11) and plastic strain in the *x*-direction (PE11) at different times during the build process. After the deposition of the first layer (Fig. 8 (a)), large longitudinal (S11) tensile stresses exist in the longer

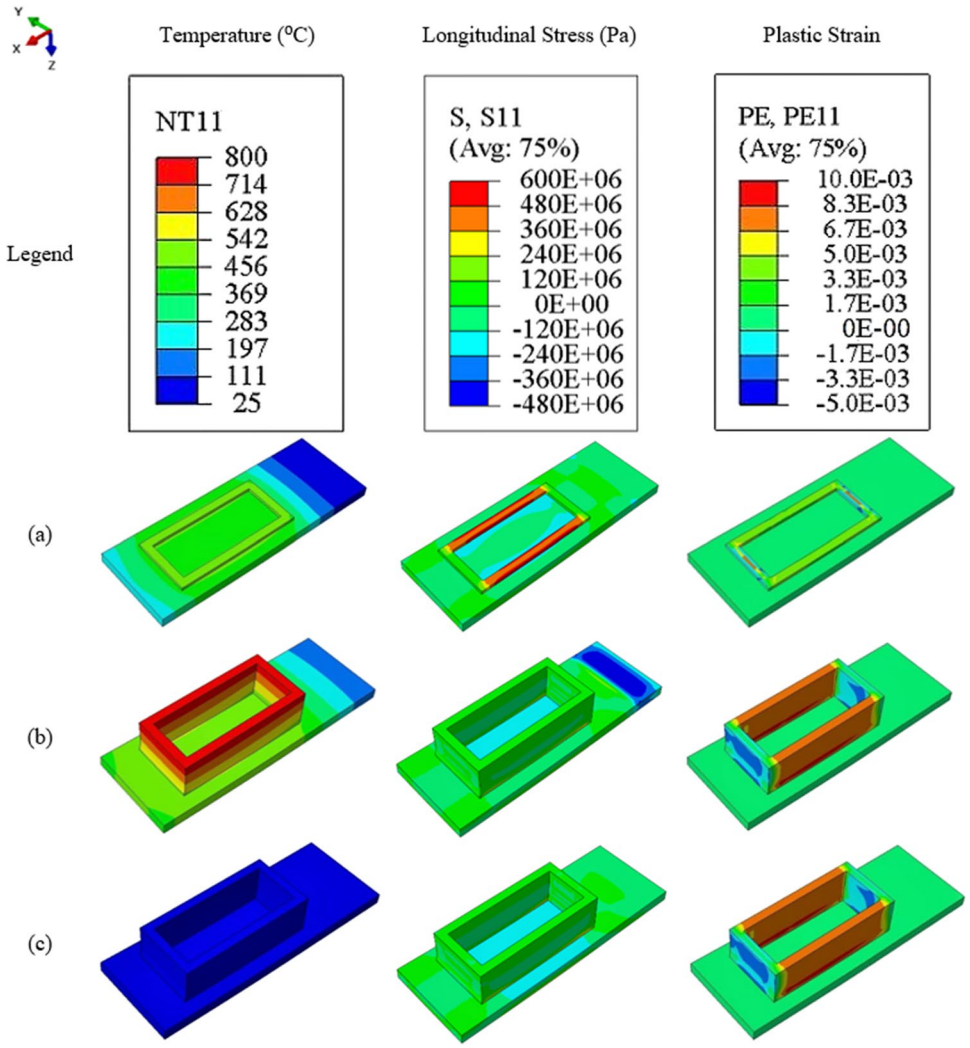

Fig. 8 The evolution of the temperature, longitudinal stress in the *x*-direction and plastic strain in the *x*-direction at (**a**) the end of the deposition of the first layer, (**b**) the end of deposition of all layers and (**c**) the end of cooling the entire part to room temperature

walls due to the difference in the accumulated thermal strain between the deposited material and the baseplate. This, in turn, leads to the build-up of positive plastic strain in the longer walls and upward deformation of the baseplate and the deposited material. At the point in the process when all layers have been deposited (Fig. 8 (b)), the magnitude of positive plastic strain in the longer wall has increased, and the magnitude of longitudinal stresses on the top of the built part has decreased. This reduction is due to the decrease in the temperature gradient between the baseplate and the new layers. The top surface of the baseplate exhibits compressive stresses due to the cooling and contraction of the deposited layers. The maximum tensile stresses occur at the interface where the deposited layers are in contact with the baseplate. After cooling the built part to room temperature (Fig. 8 (c)), negligible change was seen in plastic strain. The further contraction of the built part has led to increased compressive stress on the baseplate's top surface (the area bounded by the hollow rectangle) and caused the further displacement of the baseplate in the upwards direction. The bottom surface of the baseplate is subject to longitudinal tensile stresses resulting from force equilibrium.

The residual stresses (S22) along the midline of the baseplate's top surface (*X*-coordinate), which intersects the midpoint of the short walls, are shown in Fig. 9. The maximum tensile stress of ~ 400 MPa occurs at the interface between the baseplate and the deposited layers. The residual stresses inside the area bounded by the hollow rectangle are compressive (reaching ~ − 200 MPa) due to the shrinkage of the built part during final cooling to room temperature.

The principal plastic strain and von Mises residual stress distribution in the built part and baseplate following processing (i.e. at room temperature) are shown in Fig. 10. Maximum plastic strains are located at the interface between the baseplate and part. There is no plastic strain accumulated in the baseplate. The stresses in the part near the interface between the baseplate and part are higher relative to elsewhere in the computational domain. The maximum stresses are located at the corners of the walls, resulting from stress concentrations caused by the abrupt change in geometry and

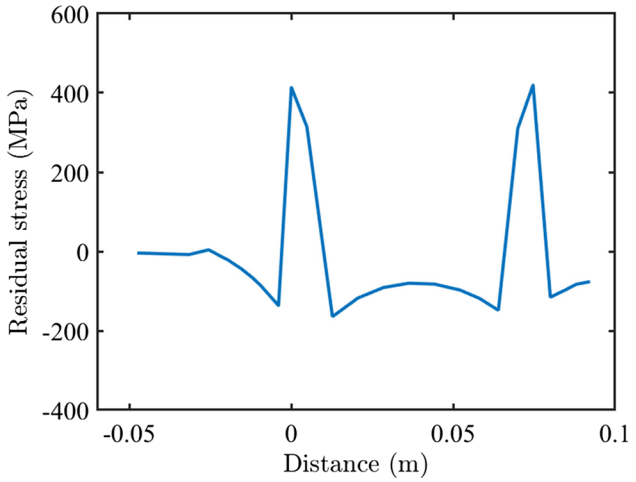

Fig. 9 The residual stress (S22) for the short walls along the midline of the top surface of the baseplate

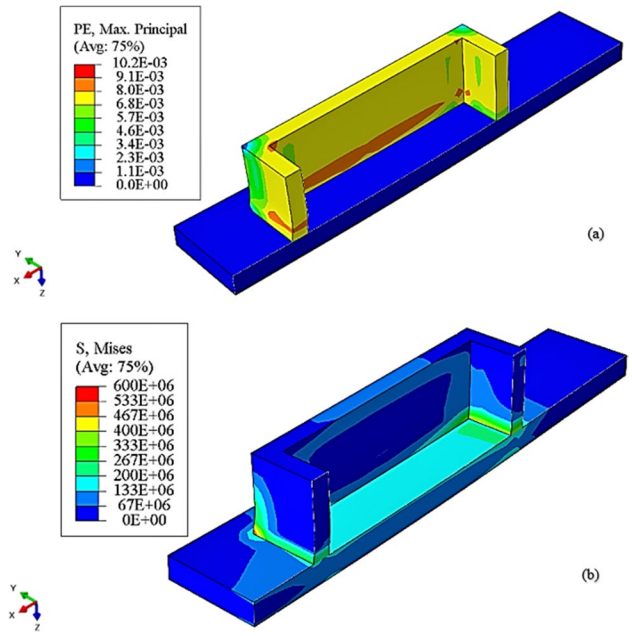

Fig. 10 (**a**)The principal plastic strains and (**b**) von Mises residual stresses at the end of the process (units for stress are in Pa)

the accumulation of strain due to the deposition of hot material on the cold baseplate.

3.3 Sensitivity analysis

A sensitivity analysis was conducted with the model to assess the impact of the initial temperature of the deposited material, heat source power and preheat temperature. In each case, the parameter being assessed was increased and/or decreased by a fixed amount, and the effects on distortion, temperature and/or thermal strain were examined. The effect of the first deposited layers compared to the last deposited layers on distortion was also investigated.

The effects of the initial temperature of the deposited material on the thermal strain evolution at a location in the first layer of the built part and the distortion evolution of the baseplate at DS1 (see Fig. 4 for location) are shown in Fig. 11. The effect of the initial temperature of the deposited material on plastic strain generation in the first layer of the deposited material is also shown in Fig. 12. Referring to the element activation description, setting the initial activation temperature above 1604 ℃ affects the temperature gradient established in the newly activated layer of elements. This effect changes the thermal stress and the amount of plastic strain formed in the newly activated layer of elements, as seen in Fig. 12. It is important to point out that this occurs despite setting the reference temperature for thermal strain accumulation at 1604 ℃ and the thermal strain accumulation above 1604 ℃ to be zero.

Figures 11 and Fig. 12 show the relative roles of thermal strain mismatch between the deposited material and the baseplate and tensile plastic strain accumulation on distortion. Figure 11 shows that as the initial temperature of deposited material increases, the amount of negative thermal strain increases. The increase in negative thermal strain should increase distortion. However, as can be seen in Fig. 11, it does not. Figure 12 shows that as the initial temperature of the deposited material increases, the tensile plastic strain also increases, which reduces the overall distortion. This approach is equivalent to introducing the inherent plastic strain. The initial temperature of the deposited material was used in this model as the main tuning parameter to align the predicted distortion with the measured distortion (see Fig. 6).

The effects of the heat source power on the temperature of the baseplate at TC3 and the distortion evolution of the baseplate at DS1 (see Fig. 4 for locations) are shown in Fig. 13. The results show that increasing the heat source power leads to a higher temperature as well as lower distortion for the baseplate. The higher heat input resulted in higher baseplate temperatures and reduced temperature gradients between the baseplate and deposited layers, leading to less distortion.

The effects of preheating the baseplate on the distortion evolution of the baseplate at DS1 and the temperature of the baseplate at TC3 (see Fig. 4 for locations) are shown in Fig. 14. As can be seen, preheating the baseplate reduces the distortion since increasing the baseplate's temperature reduces the temperature gradient between the baseplate and the first deposited layers. Furthermore, less cumulative strain or strain mismatch, i.e. a hot part on a warm baseplate compared to a hot part on a cold baseplate, can further reduce the distortion. The temperature histories for the preheat

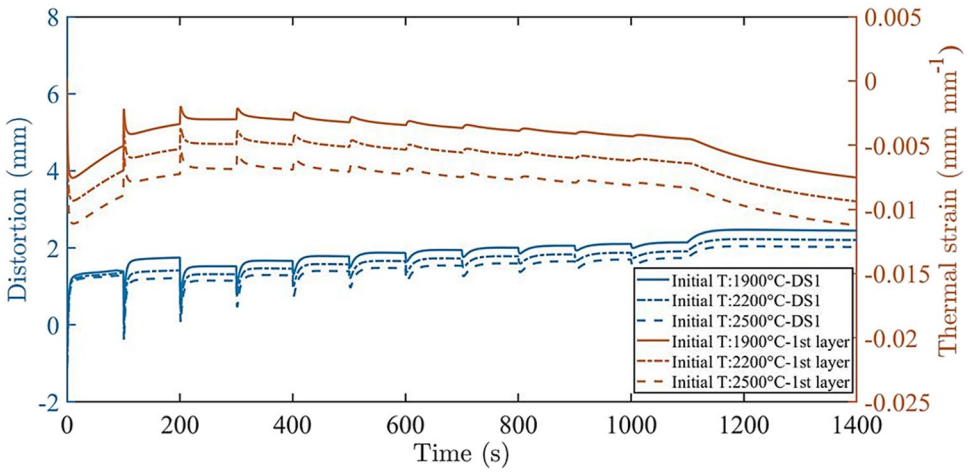

Fig. 11 The distortion evolution of the baseplate's bottom surface at DS1 and the thermal strain evolution of the first layer of the part under different initial temperatures for the deposited layer

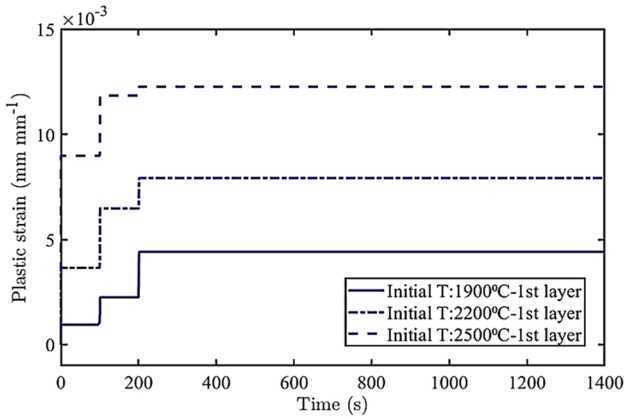

Fig. 12 The plastic strain of the first layer of the part under different initial temperatures for the deposited layer

condition indicate that initial temperature differences in the baseplate are eliminated as the build progresses.

The effect of the deposited layers on distortion can be seen in Fig. 6. During the deposition of the first layers, a significant distortion occurs in the baseplate due to the large thermal strain difference between the deposited material and the baseplate. During the deposition of the last layers, the amount of increase in distortion is smaller compared to the distortion after the deposition of the first layers. This is due to a combination of the reduced thermal gradient and thermal strain mismatch between the newly deposited layer and the previously consolidated layers.

4 Summary and conclusions

In this paper, a computationally efficient strategy has been implemented for the prediction of the thermo-mechanical behaviour of a component manufactured via the DED process. A 3D transient thermo-mechanical model was developed to predict the temperature, stress and distortion evolution in a hollow rectangular part built on a baseplate in a laser-based, powder-fed DED process. The model predictions were validated against in situ temperature and displacement data obtained from a literature-based study [11]. The validated model was also used to investigate

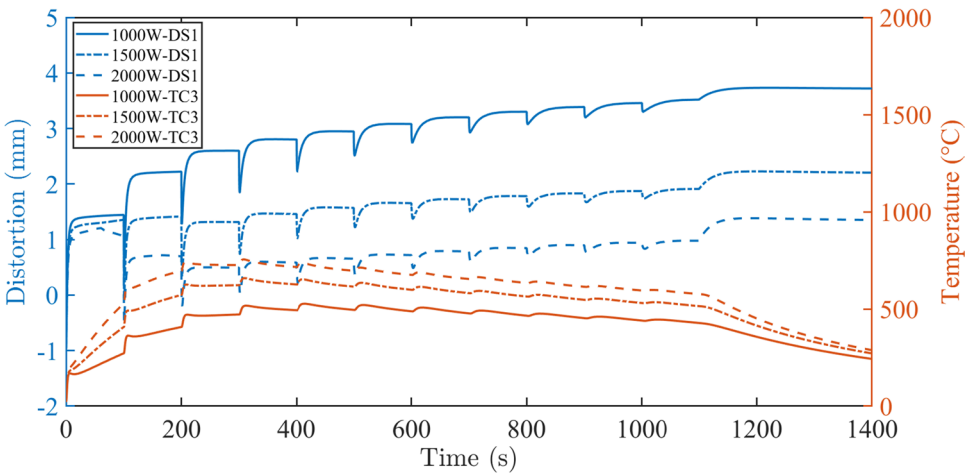

Fig. 13 The distortion evolution of the baseplate's bottom surface at DS1 and the thermal behaviour of the baseplate at TC3 under different laser powers

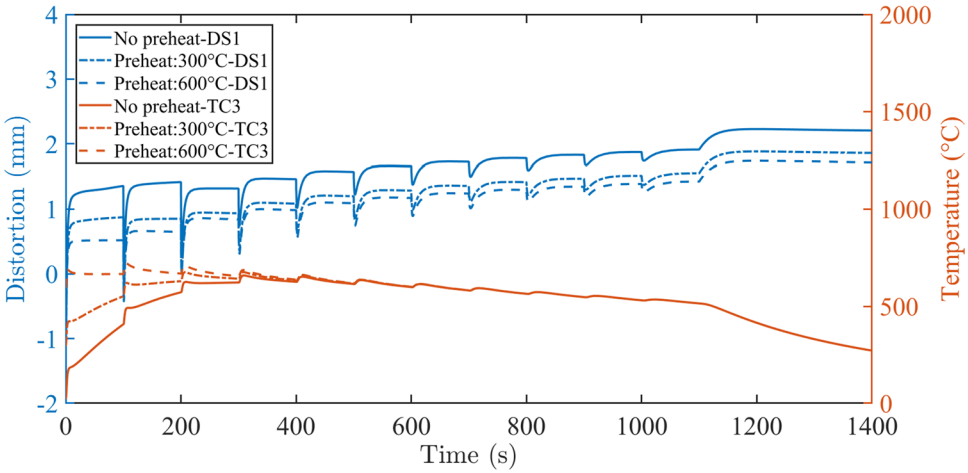

Fig. 14 The distortion evolution of the baseplate's bottom surface at DS1 and the thermal behaviour of the baseplate at TC3 under different preheat temperatures

the effect of the heat source power, the initial temperature of the deposited material and baseplate preheating on the thermal behaviour and distortion evolution. The novel features of the current modeling methodology include activating the deposited material at an initial temperature above the solidus to capture the generation of plastic strain, compensating for the enthalpy of the deposited material in the time-averaged volumetric heat input describing the laser and defining separate, material-centric, thermal strain evolution for the deposited material and the baseplate.

The predicted and measured temperature history on the bottom surface of the baseplate showed good agreement suggesting that the model is able to accurately describe the thermal conditions in the process. The model was also able to accurately predict the total displacement of the baseplate. However, the evolution of distortion predicted by the model during the initial stage of the build exhibited a different trend than the measurements. The stress predictions indicated that high stresses occur at the interface between the baseplate and the built part. Once the part had cooled, the residual stresses on the top surface of the baseplate were compressive (approximately – 200 MPa) inside the hollow rectangle due to the shrinkage of the part during final cooling to room temperature. The maximum tensile residual stresses (approximately 600 MPa) were located at the corners of the walls due to strain mismatch and the abrupt change in geometry. A sensitivity analysis showed that preheating the baseplate, increasing the heat source power and increasing the initial temperature of the deposited material reduced the baseplate distortion.

As pointed out earlier, the deposited material's initial temperature was adjusted through a trial-and-error approach to fit the predicted distortion history with the in situ displacement data by capturing the generation of plastic strain. This creates an artificial constraint on the analysis as the material deposition temperature should strictly be a function of the fraction of the beam input power transferred to the feed material, the material feed rate and the input of residual beam energy to the baseplate. To remove this constraint, future work is needed to allow the model to predict the effect of the process parameters on strain evolution, residual stresses and distortion of the component more accurately.

Author contribution Pegah Pourabdollah: conceptualization, methodology, writing — original draft, validation, formal analysis, visualization.

Farzaneh Farhang Mehr: conceptualization, formal analysis, methodology, writing — review and editing, supervising.

Daan M. Maijer: conceptualization, formal analysis, methodology, writing — review and editing, supervising, resources, project administration.

Steven L. Cockcroft: conceptualization, methodology, writing — review, supervising, resources, project administration, funding acquisition.

Funding This work was supported by NSERC-netgp-494158–2016. Steven L. Cockcroft has received research support from Natural Sciences and Engineering Research Council of Canada.

Declarations

Competing interests The authors declare no competing interests.

References

1. Frazier WE (2014) Metal additive manufacturing: a review. J Mater Eng Perform 23:1917–1928. https://doi.org/10.1007/S11665-014-0958-Z/FIGURES/9
2. Herzog D, Seyda V, Wycisk E, Emmelmann C (2016) Additive manufacturing of metals. Acta Mater 117. https://doi.org/10.1016/j.actamat.2016.07.019
3. Körner C (2016) Additive manufacturing of metallic components by selective electron beam melting - a review. Int Mater Rev 61. https://doi.org/10.1080/09506608.2016.1176289

4. Thompson SM, Bian L, Shamsaei N, Yadollahi A (2015) An overview of direct laser deposition for additive manufacturing; part I: transport phenomena, modeling and diagnostics. Addit Manuf 8. https://doi.org/10.1016/j.addma.2015.07.001
5. Liu S, Shin YC (2019) Additive manufacturing of Ti6Al4V alloy: a review. Mater Des 164. https://doi.org/10.1016/j.matdes.2018.107552
6. Li L (2006) Repair of directionally solidified superalloy GTD-111 by laser-engineered net shaping. J Mater Sci 41. https://doi.org/10.1007/s10853-006-0948-0
7. Liang X, Cheng L, Chen Q, Yang Q, To AC (2018) A modified method for estimating inherent strains from detailed process simulation for fast residual distortion prediction of single-walled structures fabricated by directed energy deposition. Addit Manuf 23. https://doi.org/10.1016/j.addma.2018.08.029
8. Mukherjee T, Zhang W, DebRoy T (2017) An improved prediction of residual stresses and distortion in additive manufacturing. Comput Mater Sci 126. https://doi.org/10.1016/j.commatsci.2016.10.003
9. DebRoy T, Wei HL, Zuback JS, Mukherjee T, Elmer JW, Milewski JO et al (2018) Additive manufacturing of metallic components – process, structure and properties. Prog Mater Sci 92:112–224. https://doi.org/10.1016/J.PMATSCI.2017.10.001
10 Sikan F, Wanjara P, Gholipour J, Kumar A, Brochu M (2021) Thermo-mechanical modeling of wire-fed electron beam additive manufacturing. Materials 14:911. https://doi.org/10.3390/MA14040911
11. Lu X, Lin X, Chiumenti M, Cervera M, Hu Y, Ji X et al (2019) Residual stress and distortion of rectangular and S-shaped Ti-6Al-4V parts by directed energy deposition: modelling and experimental calibration. Addit Manuf 26:166–179. https://doi.org/10.1016/j.addma.2019.02.001
12. Gao M, Wang Z, Li X, Zeng X (2013) The effect of deposition patterns on the deformation of substrates during direct laser fabrication. J Eng Mater Technol 135. https://doi.org/10.1115/1.4024195
13. Cao J, Gharghouri MA, Nash P (2016) Finite-element analysis and experimental validation of thermal residual stress and distortion in electron beam additive manufactured Ti-6Al-4V build plates. J Mater Process Technol 237. https://doi.org/10.1016/j.jmatprotec.2016.06.032.
14. Ganeriwala RK, Strantza M, King WE, Clausen B, Phan TQ, Levine LE et al (2019) Evaluation of a thermomechanical model for prediction of residual stress during laser powder bed fusion of Ti-6Al-4V. Addit Manuf 27. https://doi.org/10.1016/j.addma.2019.03.034
15. Biegler M, Graf B, Rethmeier M (2018) In-situ distortions in LMD additive manufacturing walls can be measured with digital image correlation and predicted using numerical simulations. Addit Manuf 20:101–110. https://doi.org/10.1016/J.ADDMA.2017.12.007
16. Zhao X, Iyer A, Promoppatum P, Yao SC (2017) Numerical modeling of the thermal behavior and residual stress in the direct metal laser sintering process of titanium alloy products. Addit Manuf 14. https://doi.org/10.1016/j.addma.2016.10.005
17. Kiran A, Hodek J, Vavřík J, Urbánek M, Džugan J (2020) Numerical simulation development and computational optimization for directed energy deposition additive manufacturing process. Materials 13. https://doi.org/10.3390/ma13112666
18. Denlinger ER, Irwin J, Michaleris P (2014) Thermomechanical modeling of additive manufacturing large parts. Journal of Manufacturing Science and Engineering, Transactions of the ASME 136. https://doi.org/10.1115/1.4028669
19. Keller N, Ploshikhin V (2014) New method for fast predictions of residual stress and distortion of AM parts. 25th Annual International Solid Freeform Fabrication Symposium &#65533; An Additive Manufacturing Conference, SFF 2014
20. Bayat M, Klingaa CG, Mohanty S, de Baere D, Thorborg J, Tiedje NS et al (2020) Part-scale thermo-mechanical modelling of distortions in laser powder bed fusion – analysis of the sequential flash heating method with experimental validation. Addit Manuf 36. https://doi.org/10.1016/j.addma.2020.101508
21. Hodge NE, Ferencz RM, Vignes RM (2016) Experimental comparison of residual stresses for a thermomechanical model for the simulation of selective laser melting. Addit Manuf 12. https://doi.org/10.1016/j.addma.2016.05.011
22. Zaeh MF, Branner G (2010) Investigations on residual stresses and deformations in selective laser melting. Production Engineering 4. https://doi.org/10.1007/s11740-009-0192-y
23. Gouge M, Michaleris P, Denlinger E, Irwin J (2018) The finite element method for the thermo-mechanical modeling of additive manufacturing processes. Thermo-Mechanical Model Addit Manuf. https://doi.org/10.1016/B978-0-12-811820-7.00003-3
24. Gouge M, Denlinger E, Irwin J, Li C, Michaleris P (2019) Experimental validation of thermo-mechanical part-scale modeling for laser powder bed fusion processes. Addit Manuf 29. https://doi.org/10.1016/j.addma.2019.06.022
25. Wang J, Zhang J, Liang L, Huang A, Yang G, Pang S (2022) A line-based flash heating method for numerical modeling and prediction of directed energy deposition manufacturing process. J Manuf Process 73:822–838. https://doi.org/10.1016/j.jmapro.2021.11.041
26. Li C, Fu CH, Guo YB, Fang FZ (2016) A multiscale modeling approach for fast prediction of part distortion in selective laser melting. J Mater Process Technol 229:703–712. https://doi.org/10.1016/J.JMATPROTEC.2015.10.022
27. Ueda Y, Fukuda K, Tanigawa M (1979) New Measuring method of 3-dimensional residual stresses based on theory of inherent strain. Journal of the Society of Naval Architects of Japan 1979:203–11. https://doi.org/10.2534/JJASNAOE1968.1979.203
28. Denlinger ER, Heigel JC, Michaleris P (2015) Residual stress and distortion modeling of electron beam direct manufacturing Ti-6Al-4V. Proc Inst Mech Eng B J Eng Manuf 229. https://doi.org/10.1177/0954405414539494
29. Thermal expansion n.d. https://abaqus-docs.mit.edu/2017/English/SIMACAEMATRefMap/simamat-c-thermalexpan.htm (accessed September 26, 2021)
30. Babu B, Lindgren LE (2013) Dislocation density based model for plastic deformation and globularization of Ti-6Al-4V. Int J Plast 50. https://doi.org/10.1016/j.ijplas.2013.04.003
31. Nemat-Nasser S, Guo WG, Nesterenko VF, Indrakanti SS, Gu YB (2001) Dynamic response of conventional and hot isostatically pressed Ti-6Al-4V alloys: experiments and modeling. Mechanics of Materials 33. https://doi.org/10.1016/S0167-6636(01)00063-1.